PI(3,4)P_2-mediated membrane tubulation promotes integrin trafficking and invasive cell migration

Zhen Feng[a] and Cheng-han Yu[a,1]

[a]School of Biomedical Sciences, Li Ka Shing Faculty of Medicine, The University of Hong Kong, Pokfulam, Hong Kong SAR, China

Edited by Sandra L. Schmid, Chan Zuckerberg Biohub, San Francisco, CA, and approved April 1, 2021 (received for review August 21, 2020)

Invadopodia are integrin-mediated adhesions with abundant PI(3,4)P_2. However, the functional role of PI(3,4)P_2 in adhesion signaling remains unclear. Here, we find that the PI(3,4)P_2 biogenesis regulates the integrin endocytosis at invadopodia. PI(3,4)P_2 is locally produced by PIK3CA and SHIP2 and is concentrated at the trailing edge of the invadopodium arc. The PI(3,4)P_2-rich compartment locally forms small puncta (membrane buds) in a SNX9-dependent manner, recruits dynein activator Hook1 through AKTIP, and rearranges into micrometer-long tubular invaginations (membrane tubes). The uncurving membrane tube extends rapidly, follows the retrograde movement of dynein along microtubule tracks, and disconnects from the plasma membrane. Activated integrin-beta3 is locally internalized through the pathway of PI(3,4)P_2-mediated membrane invagination and is then actively recycled. Blockages of PI3K, SHIP2, and SNX9 suppress integrin-beta3 endocytosis, delay adhesion turnover, and impede transwell invasion of MEF-Src and MDA-MB-231 cells. Thus, the production of PI(3,4)P_2 promotes invasive cell migration by stimulating the trafficking of integrin receptor at the invadopodium.

phosphoinositide lipids | invadopodia | integrin trafficking | microtubule

Upon binding to the extracellular matrix, the integrin receptor acts as the transmembrane anchor of cell–matrix adhesion and recruits signal regulation factors to coordinate cytoskeletal reorganization and subsequent cell motility (1, 2). Invadopodia are specialized integrin-mediated adhesions that are utilized by invasive cancer cells to migrate through tissue barriers (3, 4). The invadopodium contains a core of densely polymerized F-actin that is surrounded by integrin receptors. Matrix metalloproteinases also accumulate at the invadopodium, degrade the extracellular matrix in proximity, and support cell invasion. The dynamic distribution of integrin receptors plays important roles in adhesion formation and cell migration (5, 6). In particular, the turnover of preexisting adhesions and the assembly of new ones have critical impacts on the speed and the persistence of cell migration. Microtubule targeting to the adhesion site and the associated motor activity can stimulate the bidirectional trafficking of cell surface receptors and modulate the adhesion composition (7, 8). The endocytosis of integrin receptors can weaken the preexisting adhesion and promote the adhesion disassembly. On the other hand, the redistribution of endocytosed integrin receptors back to the plasma membrane allows the formation of new adhesion sites and further supports the cell migration (9, 10).

Phosphoinositide lipids are important signaling molecules in the plasma membrane and cytoplasmic organelles (11). The phosphorylation at the 3, 4, and/or 5 hydroxyl positions of the inositol head group can result in seven types of phosphoinositide lipids, including phosphatidylinositol monophosphate [PI(3)P, PI(4)P, and PI(5)P], diphosphate [PI(3,4)P_2, PI(3,5)P_2, and PI(4,5)P_2], and triphosphate [PI(3,4,5)P_3]. Phosphoinositide lipids with different phosphorylation states can recruit specific cytoplasmic effectors to trigger diverse cellular events, including cytoskeletal reorganization, ion channel regulation, and organelle trafficking (12). In particular, interactions between phosphoinositide lipids and bin/amphiphysin/rvs (BAR)-domain proteins can stimulate membrane curvature modulation and receptor endocytosis (13, 14). The conversions between phosphoinositide lipids may involve multiple steps and are dynamically regulated by site-specific kinases and phosphatases (15). In particular, the production of PI(3,4)P_2 can be controlled by two different pathways (16). Dephosphorylation of PI(3,4,5)P_3 by phosphoinositide 5-phosphatases can result in the production of PI(3,4)P_2 (17). On the other hand, class II PI3Ks can directly phosphorylate PI(4)P and contribute to PI(3,4)P_2 production (18).

In the invadopodium, PI(3,4,5)P_3 and PI(3,4)P_2 act as important upstream messengers to initiate F-actin polymerization (3). However, the functional role of phosphoinositide lipids in adhesion turnover and integrin trafficking at invadopodia remains unclear. Here, we use the invadopodium model system of Src-transformed fibroblast (MEF-Src) (3, 19, 20) and MDA-MB-231 breast cancer cell to reveal how the PI(3,4)P_2 production and the microtubule-mediated retrograde transport trigger the membrane tubulation, stimulate the integrin endocytosis, and promote the invasive cell migration.

Results

Asymmetrical Distribution of PI(3,4)P_2 across the Invadopodium Arc. Species-specific binding probes have been used to report the dynamic distribution of phosphoinositide lipids inside the cell (21). While the previous study and ours have reported the enrichment of PI(3,4,5)P_3 and PI(3,4)P_2 at the invadopodium using the model system of MEF-Src cells (*SI Appendix*, Fig. S1*A*) (19, 22), the distributions of these two lipids within the invadopodium were rather different. PI(3,4)P_2, visualized by the PH-Tapp1

Significance

The dynamic distribution of phosphoinositide lipids orchestrates intracellular compartmentalization and protein sorting. Here, we report the PI(3,4)P_2-dependent endocytosis of adhesion receptor integrin-beta3 at the invadopodium and its implication in promoting invasive cell migration. PI(3,4)P_2-rich compartment in the plasma membrane contains integrin-beta3 and is actively internalized through SNX9-mediated membrane invagination as well as dynein-mediated membrane tubulation along cortical microtubule tracks. Accelerated integrin endocytosis promotes adhesion turnover, and subsequent integrin exocytosis further supports cell migration. In general, the functional link between PI(3,4)P_2 biogenesis and membrane internalization can be applicable to other membrane molecules at the invadopodium and provide insights into the regulation of cell migration.

Author contributions: Z.F. and C.-h.Y. designed research, performed research, contributed new reagents/analytic tools, analyzed data, and wrote the paper.

The authors declare no competing interest.

This article is a PNAS Direct Submission.

[1]To whom correspondence may be addressed. Email: chyu1@hku.hk.

This article contains supporting information online at https://www.pnas.org/lookup/suppl/doi:10.1073/pnas.2017645118/-/DCSupplemental.

Published May 4, 2021.

probe, was asymmetrically accumulated at the trailing edge of the invadopodium arc, compared to the plasma membrane marker CAAX (Fig. 1 *A* and *D*). On the other hand, the distribution of $PI(3,4,5)P_3$, revealed by the PH-BTK probe, was homogeneously enriched across the invadopodium arc (Fig. 1 *B* and *D*). $PI(4,5)P_2$, PI(4)P, and PI(3)P, reported by PH-PLCd, P4M-SidM, and PX-p40phox probes respectively, were not distinctly enriched at the invadopodium arc (Fig. 1 *C* and *D* and *SI Appendix*, Fig. S1 *B–E*). To determine the kinase involved in the local production of $PI(3,4)P_2$ (Fig. 1*E*), we examined the subcellular localization of various PI3K catalytic subunits. Green fluorescent protein (GFP)-tagged class I PIK3CA and PIK3CB were located at the invadopodium, while PIK3CG and PIK3CD appeared to be diffusive in the cytoplasm (*SI Appendix*, Fig. S1*F*). Analyses using RT-qPCR suggested that PIK3CA, rather than PIK3CB, was the major catalytic subunit expressed in MEF-Src (*SI Appendix*, Fig. S1*G*). Class II PI3Ks, including PIK3C2A, PIK3C2B, and PIK3C2G, were not enriched at invadopodia (*SI Appendix*, Fig. S1*H*).

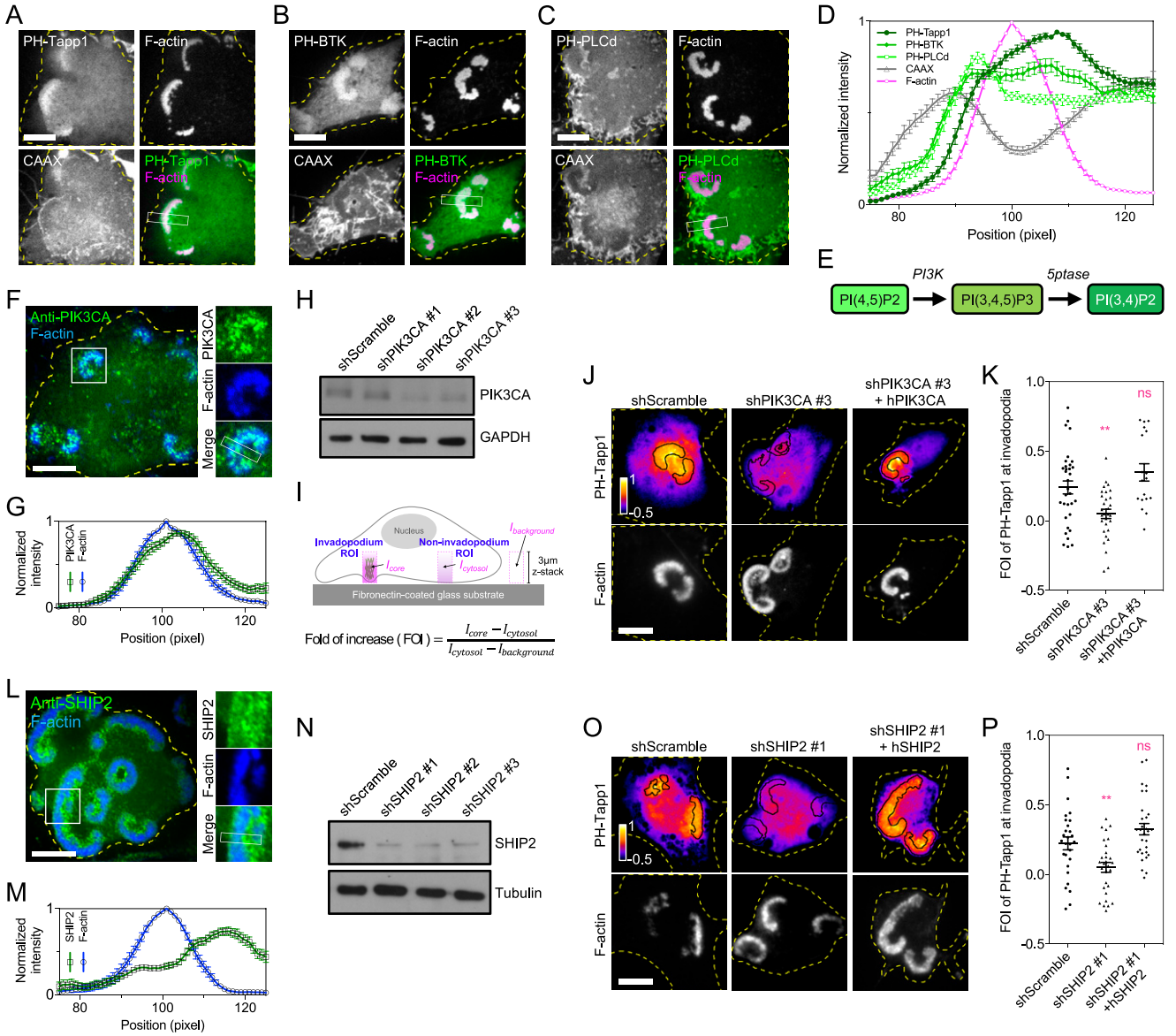

Fig. 1. $PI(3,4)P_2$ concentrates at the trailing edge of the invadopodium arc. (*A*) GFP-PH-Tapp1 (the $PI(3,4)P_2$ probe) is enriched at the trailing edge of the invadopodium arc in MEF-Src in comparison with the plasma membrane marker mCherry-CAAX. (*B*) PH-BTK-GFP (the $PI(3,4,5)P_3$ probe) is homogenously enriched within the invadopodium arc. (*C*) PH-PLCd-GFP (the $PI(4,5)P_2$ probe) is not distinctly enriched in the invadopodium arc. (*D*) The intensity profiles of PH-Tapp1, PH-BTK, PH-PLCd, CAAX, and F-actin across the invadopodium arc (outside-in line scan; $n = 21$, 38, 38, 89, and 78, respectively). (*E*) The pathway involved in the biogenesis of $PI(3,4)P_2$. (*F*) Endogenous PIK3CA is located at the invadopodium. (*G*) The intensity profiles of PIK3CA and F-actin across the invadopodium (outside-in line scan, $n = 17$). (*H*) The Western blot indicates the knockdown of PIK3CA by the shRNA. (*I*) The schematic diagram of ratiometric enrichment analysis. (*J*) The knockdown of PIK3CA reduces the FOI of mCherry-PH-Tapp1 at the invadopodium. Reintroducing PIK3CA rescues the FOI of PH-Tapp1. (*K*) The FOI of PH-Tapp1 after PIK3CA knockdown and rescue as indicated. The statistical information is in *SI Appendix*, Table S1*A*. (*L*) Endogenous SHIP2 is located at the invadopodium and concentrates at the trailing edge of the invadopodium arc. (*M*) The intensity profiles of SHIP2 and F-actin across the invadopodium (outside-in line scan, $n = 23$). (*N*) The Western blot indicates the knockdown of SHIP2 by the shRNA. (*O*) The knockdown of SHIP2 reduces the FOI of mCherry-PH-Tapp1 at the invadopodium. Reintroducing SHIP2 rescues the FOI of PH-Tapp1. (*P*) The FOI of PH-Tapp1 after SHIP2 knockdown and rescue as indicated. The statistical information is in *SI Appendix*, Table S1*B*. The invadopodium arc is labeled by F-actin marker EBFP2-UtrCH. All experiments have been independently repeated three times. The graphs show mean ± SEM. One-way ANOVA with Dunnett's test is used for the statistical analysis. Ns, $P > 0.1234$; $^{**}P < 0.0021$ (Scale bars, 10 μm).

Knockdown of PIK3CA Suppresses the Production of PI(3,4)P_2. Endogenous PIK3CA concentrated at the invadopodium (Fig. 1*F*). In addition, PIK3CA showed moderate enrichment at the trailing edge of invadopodium arc (Fig. 1*G*). We next investigated whether loss of PIK3CA affects the PI(3,4)P_2 production. The knockdown of PIK3CA expression was achieved by short hairpin RNA (shRNA) (Fig. 1*H*). The impact of PIK3CA knockdown on the phosphoinositide production was quantified by the confocal microscopy and the ratiometric image analysis (*Materials and Methods*). The fold of increase (FOI) of the phosphoinositide binding probe inside a three-dimensional volume of the invadopodium (3 μm in height) was determined (Fig. 1*I*). While the formation of the invadopodium arc was not disrupted by the PIK3CA knockdown, the FOIs of PH-Tapp1 and PH-BTK were the significantly decreased in comparison with the control (Fig. 1 *J* and *K* and *SI Appendix*, Fig. S1 *I* and *J*). Reintroducing the resistant form of PIK3CA restored the enrichment of PH-Tapp1 and PH-BTK in the knockdown cells. The treatment with PIK3CA inhibitor A66 (100 nM) also resulted in similar decreases in the FOI of PH-Tapp1 and PH-BTK in comparison with the dimethyl sulfoxide (DMSO) control (*SI Appendix*, Fig. S1 *K–N*) (23). It appears that PIK3CA is the key kinase related to the production of PI(3,4,5)P_3 and PI(3,4)P_2 at the invadopodium.

SHIP2 Is the Major Phosphoinositide 5-Phosphatase to Produce PI(3,4)P_2 at the Invadopodium. As PI(3,4,5)P_3 is the leading source of PI(3,4)P_2 production on the plasma membrane (24), we sought to determine the major phosphoinositide 5-phosphatase involved (Fig. 1*E*). Among the nine phosphatases examined, SHIP2, INPP5E, SYNJ2, SHIP1, and INPP5J were enriched at invadopodia, while INPP5K, SYNJ1, INPP5B, and OCRL1 were not (*SI Appendix*, Fig. S2*A*). In particular, the endogenous expression of SHIP2 (also known as INPPL1) was high, and ectopically introduced SHIP2 greatly promoted the FOI of PH-Tapp1 (*SI Appendix*, Fig. S2 *A* and *B*). Endogenous SHIP2 was located at the trailing edge of the invadopodium arc (Fig. 1*L*). The asymmetrical distribution of SHIP2 remarkably resembled that of PH-Tapp1 (Fig. 1*M*). When SHIP2 was knocked down by the shRNA (Fig. 1*N*), the formation of the invadopodium arc in MEF-Src was not disrupted. However, the FOI of PH-Tapp1 in the invadopodium dropped significantly in comparison with the control (Fig. 1 *O* and *P*). At the same time, the FOI of PH-BTK in the invadopodium rose (*SI Appendix*, Fig. S2 *C* and *D*). Reintroducing the resistant form of SHIP2 in the knockdown cells reversed the changes of PH-Tapp1 and PH-BTK, respectively. Likewise, when the SHIP2 phosphatase activity was inhibited by AS1949490 (10 μM) (25), the lower FOI of PH-Tapp1 and the higher FOI of PH-BTK were also observed compared to the DMSO control (*SI Appendix*, Fig. S2 *E–H*). These data suggest that SHIP2 is the major phosphoinositide 5-phosphatase which contributes to the production and the asymmetrical distribution of PI(3,4)P_2 across the invadopodium arc.

PI(3,4)P_2-Rich Compartment Actively Develops into Invaginated Membrane Tubes and Endocytic Vesicles. The local production of PI(3,4)P_2 has been reported in various endocytosis events (26, 27). At the trailing edge of the invadopodium arc, we found that the PI(3,4)P_2 reporter PH-Tapp1 was further enriched at the invaginated small puncta (membrane buds) (Fig. 2 *A* and *B* and Movie S1). The PI(3,4,5)P_3 probe PH-BTK and clathrin light chain were not observed at the membrane bud (*SI Appendix*, Fig. S3 *A* and *B*). The enrichment of PI(3,4)P_2 at the membrane bud was also confirmed by the specific recruitment of other PI(3,4)P_2 reporters, including PX-Tks5 and INPP4A (*SI Appendix*, Fig. S3 *C–F*). Over time, the invaginated membrane buds broke away from the plasma membrane. Intriguingly, a population of the membrane buds extended inwardly and then formed micrometer-long straight membrane tubulations (membrane tubes) (Fig. 2*B*). The elongation rate of membrane tubes ranged from 20 to 160 nm/s (Fig. 2*C*).

We next used the glycophosphatidylinositol (GPI)-based outer leaflet membrane marker (CD52, amino acid 1 to 24) to monitor the membrane sorting. We found that mCherry-GPI was incorporated into the membrane bud and the growing membrane tube (Fig. 2 *D–F* and Movie S2). The fully grown GPI-positive membrane tube gradually lost the association of PH-Tapp1 and was detached from the plasma membrane (Fig. 2 *E* and *F*, t_2). Early endosome marker Rab5 was located further behind the invadopodium arc (Fig. 2*G* and Movie S3). The detached membrane tube with diminished PH-Tapp1 association was subsequently sorted into Rab5-positive endosomes (Fig. 2 *H* and *I*).

Microtubule and Dynein Complex Control the Growth of Membrane Tubes. The repetitive formation of straight membrane tubes at the same location behind the invadopodium arc implied the involvement of nondiffusible cytoskeletal factors. We found that the transitions from the membrane bud, the membrane tube, to the internalized vesicle took place when the microtubule reached the inner part of the invadopodium arc (Fig. 2*J* and Movie S4). Kank2, the adaptor protein connecting integrin-mediated adhesions and microtubule tips, was located at the invaginated membrane bud (*SI Appendix*, Fig. S3 *G* and *H*). In addition, the direction of tube elongation and subsequent vesicle movement followed the orientation of the microtubule in proximity. When the microtubule assembly was inhibited by nocodazole (10 μM) (*SI Appendix*, Fig. S3*I*), the formation of membrane tubes was greatly inhibited compared to the DMSO control (Fig. 2 *K* and *L*, arrowheads).

We next investigated microtubule-associated factors involved in the rapid extension of the membrane tube. p150Glued, the subunit of the microtubule motor dynactin/dynein complex (28), was found at the invaginated membrane bud (*SI Appendix*, Fig. S3 *J* and *K*). Similarly, Arp1, another subunit of the dynactin/dynein complex, stayed at the tip of growing membrane tube (Fig. 3 *A–C* and Movie S5). F-actin, on the other hand, was initially limited at the base of the membrane tube during the inward extension phase (Fig. 3*B*, before t_0) and later began to polymerize around the grown membrane tube (Fig. 3*B*, between t_0 and t_1). We sought to determine the functional adaptors of dynein that specifically targeted on PI(3,4)P_2-rich membrane buds. Hook1, the activating adaptor of dynein (29), and its binding partner AKT-interacting protein (AKTIP, also known as FTS) (30, 31) were both located at PH-Tapp1–positive membrane buds (Fig. 3 *D* and *E*). In particular, AKTIP became progressively enriched along the growing membrane tube (Fig. 3 *F–H* and Movie S6). When AKTIP was knocked down by the shRNA, Hook1 became absent from PH-Tapp1–positive membrane buds, and the formation of membrane tube was not observed (Fig. 3 *I* and *J*). Intriguingly, knockdown of AKTIP resulted in the pronounced accumulation of stationary PH-Tapp1 vesicles behind the invadopodium arc (Fig. 3*K*). When the arginine residues in the putative membrane-binding domain of AKTIP were mutated to alanine (R168A and R169A) (32), AKTIP-2RA was not recruited to PH-Tapp1–positive membrane buds (Fig. 3*K* and *SI Appendix*, Fig. S3*L*). Reintroducing the wild-type AKTIP, rather than AKTIP-2RA, reduced the number of stationary PH-Tapp1 vesicles behind the invadopodium arc (Fig. 3 *K* and *L*). Thus, dynein and its adaptor AKTIP promote the membrane tubulation along the microtubule, and additional endocytic factors should also be involved in triggering the internalization of PI(3,4)P_2-rich membrane component.

SNX9 Is a PI(3,4)P_2 Effector and Promotes the Membrane Invagination. BAR-domain proteins are known to sense and to generate the membrane curvature. Specifically, we found that PX-BAR–domain protein SNX9 was enriched at PH-Tapp1–positive membrane buds and colocalized with DNM2, the key protein involved in membrane fission (Fig. 4*A*). Other BAR-domain proteins, such as

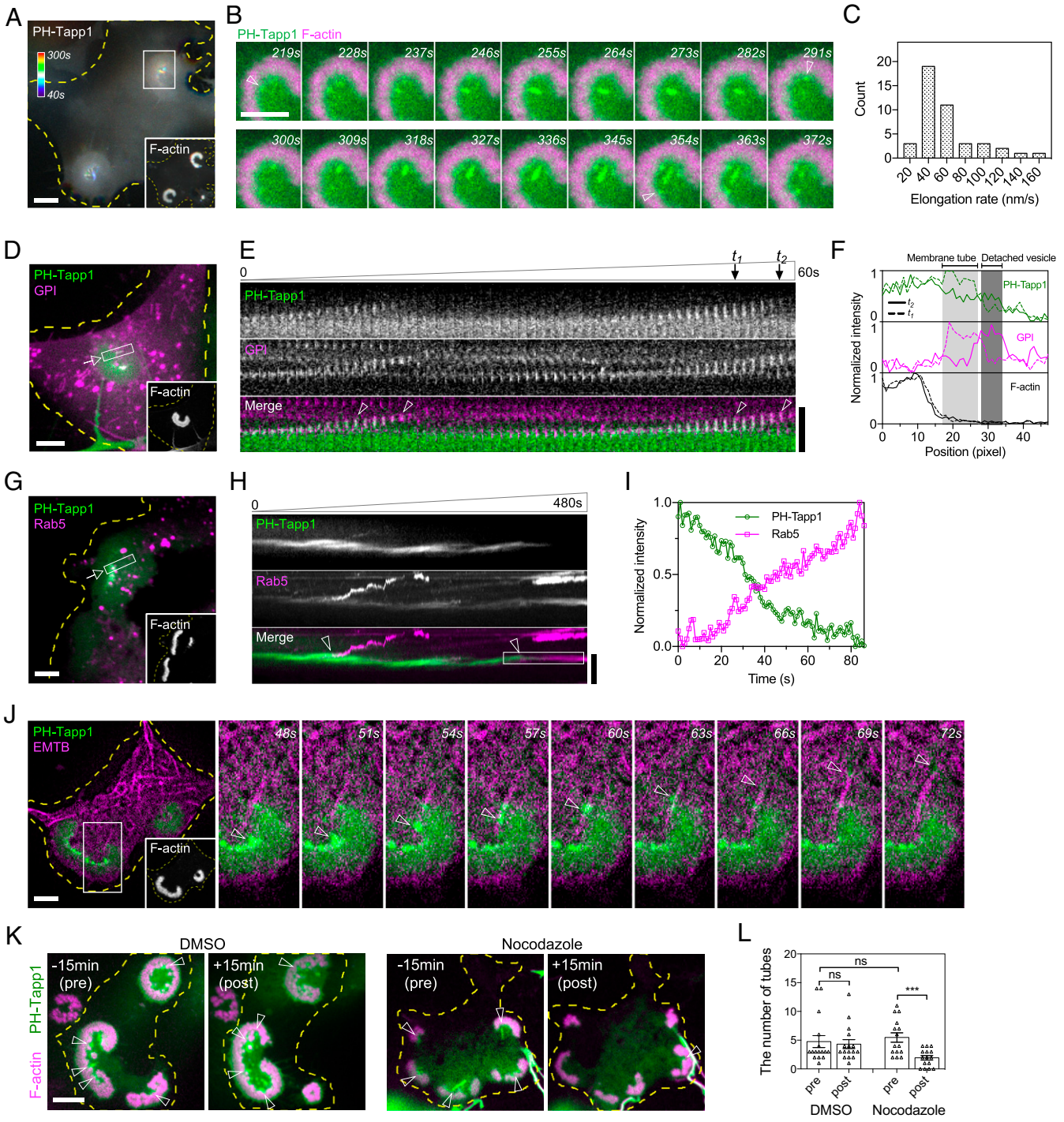

Fig. 2. PI(3,4)P_2-rich compartment forms the invaginated membrane bud and tube along cortical microtubule tracks. (*A*) Time-projected images of GFP-PH-Tapp1 and F-actin in MEF-Src (40 to 300 s, color coded). Over time, there are numerous PH-Tapp1–positive membrane invaginations behind the invadopodium arc. (*B*) Time-lapse images of the boxed region in *A* (6×8 μm^2). PH-Tapp1 puncta (membrane buds, arrowheads) initially appear at the trailing edge of the invadopodium arc, elongate inwardly, and become straight tubular membrane structures (membrane tubes). See Movie S1. (*C*) The histogram of the membrane tube elongation rate ($n = 43$). (*D*) Membrane marker GPI-mCherry colocalizes with GFP-PH-Tapp1 in the membrane tube. See Movie S2. (*E*) Time-lapse images of the boxed region of *D* (1×6 μm^2; the arrow indicates the base of the tube). Membrane tubes are repeatedly formed and then detached from the same location behind the invadopodium arc (arrowheads). (*F*) The intensity profiles of PH-Tapp1 and GPI at t_1 (the fully grown tube) and t_2 (the detached tube) in *E*. (*G*) Early endosome marker GFP-Rab5 accumulates in the vesicular compartment behind the mCherry-PH-Tapp1–labeled invadopodium arc. See Movie S3. (*H*) The kymograph along the boxed region of *G* (the arrow indicates the base of the tube). Rab5 dynamically associates with the detached membrane compartment (arrowheads). (*I*) The temporal intensity changes of PH-Tapp1 and Rab5 in the boxed region of *H*. (*J*) The GFP-PH-Tapp1–positive membrane bud elongates, breaks away from the invadopodium arc and moves along EMTB-mCherry–labeled microtubule track (arrowheads). The rectangular *Inset* shows the time-lapse images of the boxed region (6×18 μm^2). See Movie S4. (*K*) After 15 min of the nocodazole treatment (10 μM), the formation of the GFP-PH-Tapp1–positive membrane tubes is greatly suppressed compared to the DSMO control. (*L*) The number of membrane tubes within the 15 min before and after the treatment as indicated ($n = 16$ and 15). The statistical information is in *SI Appendix*, Table S1C. The invadopodium arc is labeled by F-actin marker LifeAct-mRuby (in *A* and *B*) or EBFP2-UtrCH (in *D*, *E*, *G*, *H*, *J*, and *K*). All experiments have been independently repeated three times. Unpaired two-tailed Student's *t* test is used for the statistical analysis. Ns, $P > 0.1234$; ***$P < 0.0002$ (Scale bars, 5 μm).

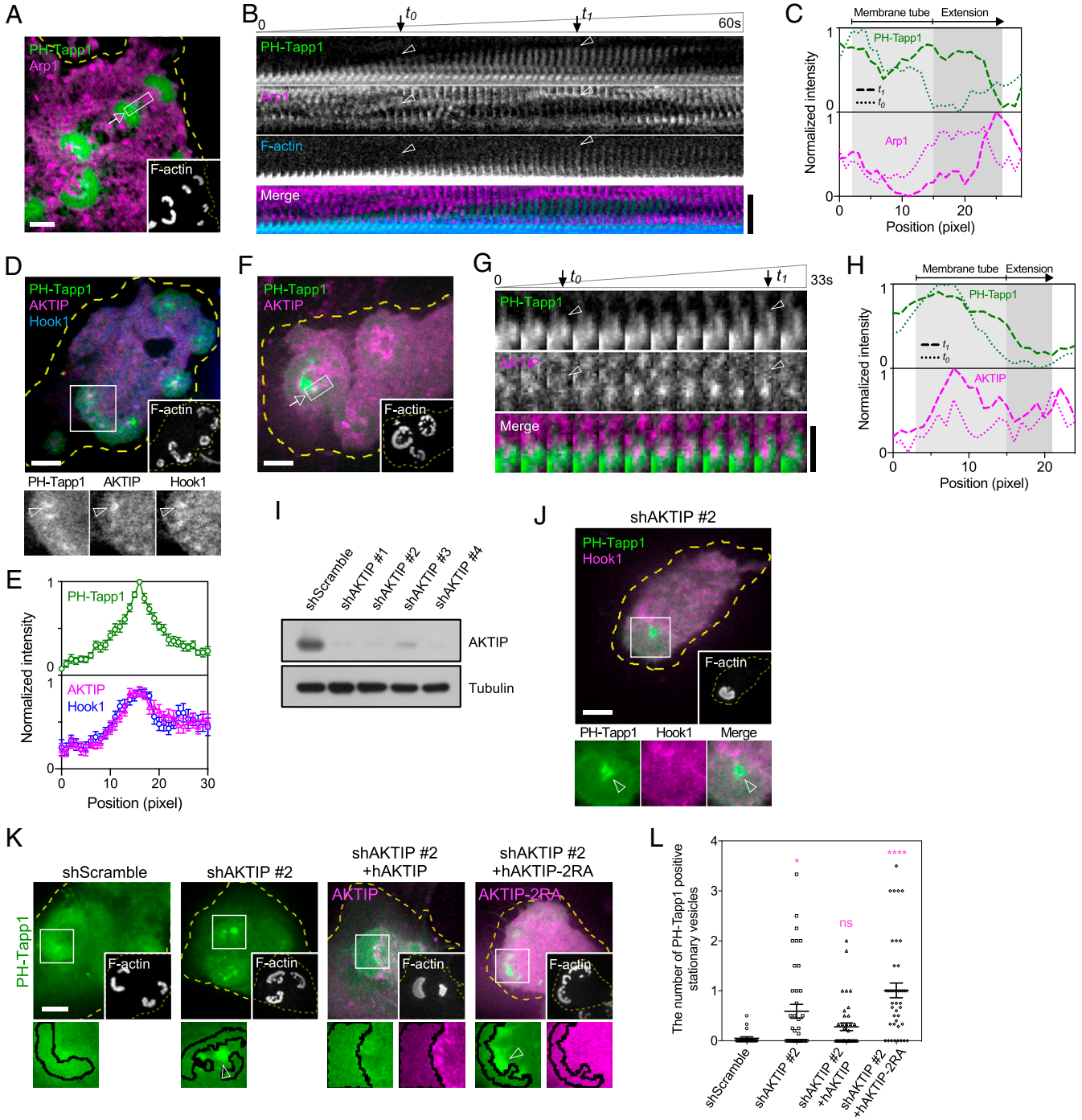

Fig. 3. Dynein and AKTIP/Hook1 complex regulate the formation of the PI(3,4)P_2-rich membrane tube. (*A*) mCherry-Arp1 is located at the tip of the GFP-PH-Tapp1–positive membrane tube. See Movie S5. (*B*) Time-lapse images of the boxed region in *A* (1 × 6 μm^2; the arrow indicates the base of the tube). (*C*) The intensity profiles of PH-Tapp1 and Arp1 at t_0 (the initial tube formation) and t_1 (the fully-grown tube) in *B*. (*D*) mCherry-AKTIP colocalizes with Hook1-GFP at the EBFP2-PH-Tapp1–positive membrane bud. (*E*) The intensity profiles of PH-Tapp1, AKTIP, and Hook1 along the arrowhead in the *Inset* of *D* (outside-in line scan, $n = 11$). (*F*) GFP-AKTIP colocalizes along the mCherry-PH-Tapp1–positive membrane tube. See Movie S6. (*G*) Time-lapse images of the boxed region in F (1.5 × 3.3 μm^2; the arrow indicates the base of the tube). (*H*) The intensity profiles of PH-Tapp1 and AKTIP at t_0 (the initial tube formation) and t_1 (the fully-grown tube) in *G*. (*I*) The Western blot indicates the knockdown of AKTIP by the shRNA. (*J*) Hook1-GFP becomes absent from the mCherry-PH-Tapp1–positive membrane bud when AKTIP is knocked down. (*K*) Knockdown of AKTIP results in the accumulation of stationary mCherry-PH-Tapp1–positive vesicles behind the invadopodium arc (arrowhead in the *Inset*). Reintroducing AKTIP, rather than putative membrane-binding mutant AKTIP-2RA, overturn the vesicle accumulation. (*L*) The number of PH-Tapp1–positive stationary vesicles (larger than 500 nm) per invadopodium arc as indicated. The statistical information is in *SI Appendix*, Table S1*D*. The invadopodium arc is labeled by F-actin marker EBFP2-UtrCH. All experiments have been independently repeated three times. The graphs show mean ± SEM. One-way ANOVA with Dunnett's test is used for the statistical analysis. Ns, $P > 0.1234$; *$P < 0.0332$; ****$P < 0.0001$ (Scale bars, 5 μm).

endophilin A1 (N-BAR), AMPH1 (N-BAR), CIP4 (F-BAR), and IRSp53 (I-BAR) did not colocalize with PH-Tapp1–positive membrane buds (*SI Appendix*, Fig. S4 *A–D*). The overexpression of SNX9 was known to spontaneously trigger membrane tubulations (33). Therefore, SNX9 was weakly expressed in order to examine its spatiotemporal role in the biogenesis of the $PI(3,4)P_2$-rich membrane tube. We found that the lipid-binding PX-BAR domain of SNX9 (201 to 595), rather than the SH3 domain (1 to 60), was sufficient to be recruited to membrane buds (*SI Appendix*, Fig. S4 *E–J*). During the membrane tube extension, full-length SNX9 and DNM2 stayed at the base of the membrane tube and subsequently dissociated as the membrane tube disconnected from the invadopodium (Fig. 4 *B* and *C*, between t_1 and t_2, and Movie S7).

We next investigated whether the recruitment of SNX9 depends on $PI(3,4)P_2$. When the $PI(3,4)P_2$ production was blocked by SHIP2 knockdown, the FOI of SNX9 at the invadopodium was suppressed (Fig. 4 *D* and *E*). Reintroducing the resistant form of SHIP2 recovered the recruitment of SNX9 in the knockdown cells. Likewise, we asked whether the formation of invaginated membrane buds is regulated by SNX9. We found that the knockdown of SNX9 greatly suppressed the number of PH-Tapp1–positive membrane buds, while the formation of the invadopodium arc was not disrupted (Fig. 4 *F–H*). Reintroducing the resistant form of SNX9 reversed the inhibitory effect in the knockdown cells. The direct association between the SH3 domain of SNX9 and the PRD domain of DNM2 was reported previously (34). Therefore, we asked whether SNX9 also regulates the recruitment of DNM2 to the $PI(3,4)P_2$-rich compartment. DNM2 without PRD domain (1 to 742) was not enriched at the membrane bud and exhibited a diffusive pattern within the

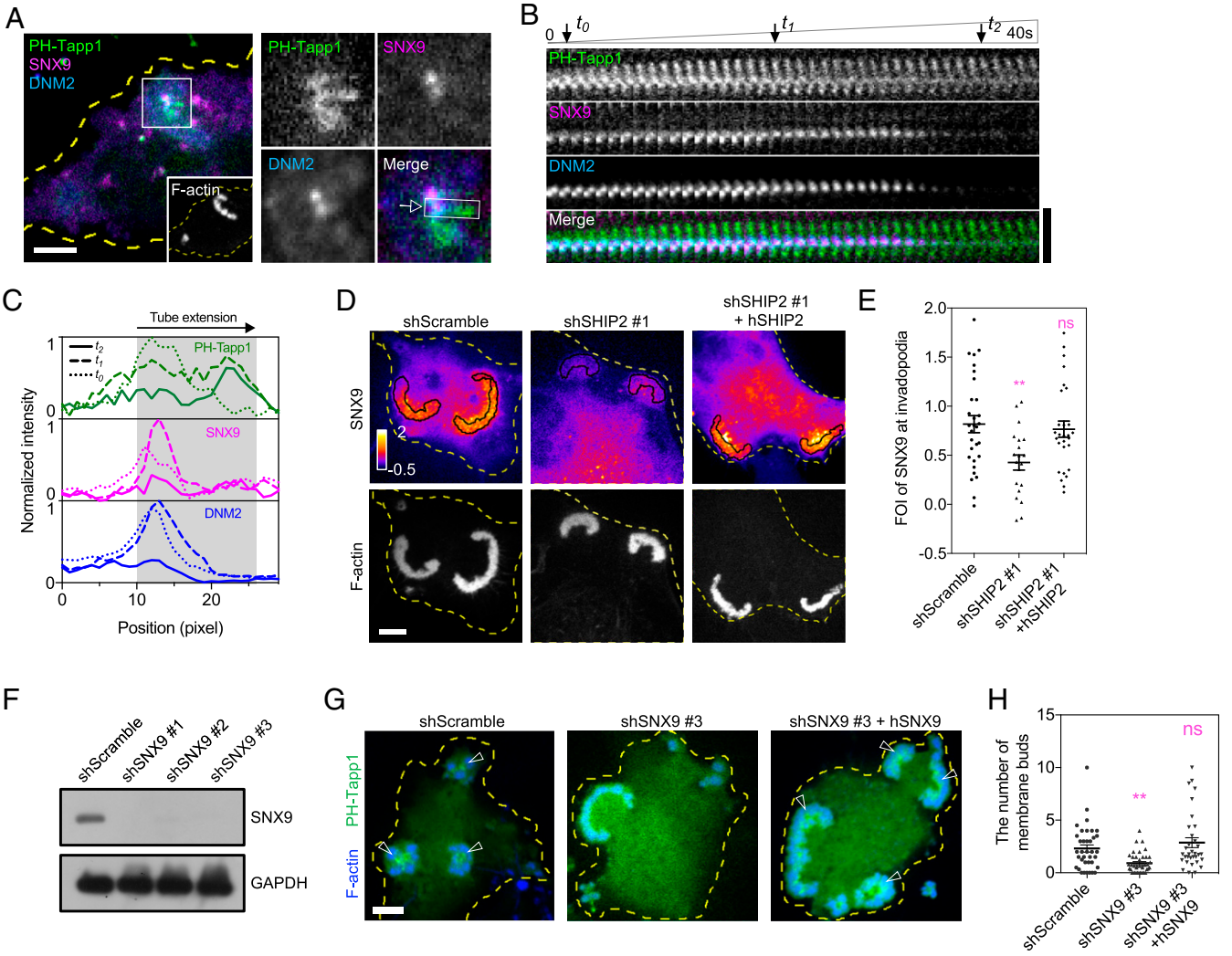

Fig. 4. $PI(3,4)P_2$ effector SNX9 regulates the membrane invagination in the trailing edge of the invadopodium arc. (*A*) mCherry-SNX9 and DNM2-GFP colocalize at the base of the EBFP2-PH-Tapp1–positive membrane tube in MEF-Src. The *Inset* shows the boxed region ($8 \times 8\ \mu m^2$). See Movie S7. (*B*) Time-lapse images of the boxed region in the *Inset* of *A* ($1 \times 6\ \mu m^2$; the arrow indicates the base of the tube). SNX9 and DNM2 colocalize at the membrane bud (t_0) and the base of membrane tube (t_1). As the membrane tube is detached from the invadopodium arc (t_2), SNX9 and DNM2 gradually dissociate. (*C*) The intensity profiles of PH-Tapp1, SNX9, and DNM2 at t_0, t_1, and t_2 in *B*. (*D*) The knockdown of SHIP2 reduces the FOI of mCherry-SNX9 at the invadopodium. Reintroducing SHIP2 restores the enrichment of SNX9. (*E*) The FOI of SNX9 after SHIP2 knockdown and rescue as indicated. The statistical information is in *SI Appendix*, Table S1*E*. (*F*) Western blot indicates the knockdown of SNX9 by the shRNA. (*G*) The knockdown of SNX9 reduces the amount of GFP-PH-Tapp1–positive membrane buds behind invadopodia. Reintroducing SNX9 restores the formation of membrane buds. (*H*) The number of PH-Tapp1–positive membrane buds per invadopodium arc after SNX9 knockdown and rescue as indicated. The statistical information is in *SI Appendix*, Table S1*F*. The invadopodium arc is labeled by F-actin marker LifeAct-miRFP703 (in *A*) or EBFP2-UtrCH (in *D* and *G*). All experiments have been independently repeated three times. The graphs show mean ± SEM. One-way ANOVA with Dunnett's test is used for the statistical analysis. Ns, $P > 0.1234$; $^{**}P < 0.0021$ (Scale bars, 5 μm).

cell (*SI Appendix*, Fig. S4*K*). The recruitment of full-length DNM2 to the trailing edge of the invadopodium was also suppressed when SNX9 was knocked down (*SI Appendix*, Fig. S4 *L* and *M*). Thus, SNX9 is the effector of $PI(3,4)P_2$ and regulates the membrane invagination and DNM2 recruitment at the trailing edge of the invadopodium.

Invadopodia Stimulate the Trafficking of Integrin-beta3 Receptor. Adhesion receptors, such as integrins, play essential roles in the assembly of invadopodia. We found that integrin-beta3 concentrated at the $PI(3,4)P_2$-rich plasma membrane invagination when MEF-Src adhered on the fibronectin-coated substrate (Fig. 5*A*). We asked whether the formation of invadopodium promotes integrin-beta3 endocytosis. As endocytosed integrin-beta3 from the plasma membrane can retain the ligand-activated conformation (5, 9), we used the conformation-specific antibody LIBS2, which recognized the exposed ectodomain of activated integrin-beta3, to examine the integrin-beta3 endocytosis. Indeed, the level of endocytosed integrin-beta3 in the cytoplasm of invadopodium-positive MEF-Src was distinctly higher than that in wild-type MEF (Fig. 5 *B* and *C*). We next investigated whether the exocytosis level of integrin-beta3 also increases. The pulse–chase assay was used to evaluate the exocytosis of integrin-beta3 (*Materials and Methods*). The conformation-specific antibody LIBS2 was used to prelabel integrin-beta3 on the cell surface and was subsequently internalized. After the serum stimulation, the exocytosis level of LIBS2-labeled integrin-beta3 in MEF-Src was indeed higher than that in wild-type MEF (Fig. 5 *D* and *E*). It appears that the invadopodium formation positively regulates the endocytosis and recycling of integrin-beta3.

$PI(3,4)P_2$-Mediated Membrane Invagination Promotes the Internalization of Integrin-beta3 and the Adhesion Turnover. As integrin-beta3 receptors were incorporated in the invaginated membrane tube, we sought to determine the role of $PI(3,4)P_2$ biogenesis in integrin-beta3 endocytosis. We found that internalized integrin-beta3 colocalized with autophosphorylated FAK (pY397-FAK) in the endosomal compartment (Fig. 5 *F* and *G*). The endosomal pY397-FAK level can be examined by Western blot and used as a surrogate of integrin endocytosis when the other contribution of pY397-FAK from the cell–matrix adhesion site was quenched by cell detachment (Fig. 5*H*) (5, 9). Indeed, the higher endosomal level of pY397-FAK was observed in MEF-Src, rather than in MEF (Fig. 5*I*), and confirmed the higher level of endocytosed integrin-beta3 (Fig. 5 *B* and *C*). The treatment with endocytosis inhibitor dynasore (20 μM) (35), as the negative control, eliminated the endosomal pY397-FAK level in the detached MEF-Src but did not alter the overall pY397-FAK level in the attached MEF-Src (Fig. 5*I* and *SI Appendix*, Fig. S5*A*). When the $PI(3,4)P_2$-mediated membrane invagination was blocked by PIK3CA, SHIP2, and SNX9 knockdown, the endosomal pY397-FAK level was significantly reduced compared to the scramble control (Fig. 5 *J*–*L*). Reintroducing PIK3CA, SHIP2, or SNX9 in the respective knockdown condition restored the endosomal pY397-FAK level (*SI Appendix*, Fig. S5*B*). The inhibition with A66 (100 nM) and AS1949490 (10 μM) also suppressed the pY397-FAK level in the detached MEF-Src, rather than that in the attached MEF-Src (*SI Appendix*, Fig. S5 *A*, *C*, and *D*). In agreement with the observation of endocytic vesicle accumulation, the endosomal pY397-FAK level remained elevated when AKTIP was knocked down (*SI Appendix*, Fig. S5*E*). Thus, $PI(3,4)P_2$-mediated membrane invagination, rather than dynein-mediated membrane tubulation, is essential to promote the endosomal pY397-FAK level and integrin endocytosis.

As up-regulated integrin endocytosis can promote the turnover of the preexisting adhesion structure, we next utilized photoconvertible mEOS2-tagged integrin-beta3 to examine the functional impact of $PI(3,4)P_2$-mediated integrin-beta3 endocytosis in the adhesion stability. After a single photoactivation by the total internal reflection fluorescence (TIRF) microscopy, the intensity changes of photoconverted integrin-beta3-mEOS2 at the invadopodium were monitored over time. We found that the intensity declines of photoconverted integrin-beta3-mEOS2 in MEF-Src were significantly slower in PIK3CA, SHIP2, and SNX9 knockdown MEF-Src compared to the scramble control (Fig. 5 *M* and *N*). In agreement with the observation of elevated endosomal pY397-FAK level, both AKTIP-knockdown and control MEF-Src exhibited fast intensity declines of photoconverted integrin-beta3-mEOS2 (*SI Appendix*, Fig. S5 *F* and *G*). Altogether, these data indicate that the $PI(3,4)P_2$ production and the SNX9-mediated membrane invagination positively stimulate the integrin-beta3 endocytosis and promote the adhesion turnover.

Suppression of $PI(3,4)P_2$-Mediated Integrin Endocytosis Impedes the Invasive Migration of MEF-Src and MDA-MB-231 Cells. Invadopodium-forming cells, such as MEF-Src and MDA-MB-231 cell, can actively penetrate and migrate through the matrix barrier. We asked whether the invasive cell migration depends on the $PI(3,4)P_2$-mediated integrin endocytosis. With the fetal bovine serum (FBS) as the chemoattractant, MEF-Src, rather than nontransformed MEF, showed the greater ability to migrate through a Matrigel-coated transwell chamber (Fig. 6 *A* and *B*). The knockdown of PIK3CA, SHIP2, and SNX9, which suppressed the $PI(3,4)P_2$-mediated integrin endocytosis, effectively impeded the transwell migration of MEF-Src (Fig. 6 *C* and *D*). Reintroducing PIK3CA, SHIP2, or SNX9 in the respective knockdown condition restored the invasive capacity. On the other hand, MEF-Src with AKTIP knockdown increasingly suffered from cell death (30), and their transwell migrations were not quantified. Likewise, MDA-MB-231 cells assemble the invadopodium and exhibit high activities of PIK3CA and PIK3CB (36, 37). We found that PH-Tapp1, SHIP2, and SNX9 also concentrated at the invadopodium of MDA-MB-231 cells (Fig. 6 *E*–*G*). The knockdown of SHIP2 and SNX9 attenuated their transwell migration abilities (Fig. 6 *H*–*K*). Rescues of SHIP2 or SNX9 in each respective knockdown condition restored the invasion capacity. Similarly, the treatment with wortmannin (200 nM, pan PI3K inhibitor) and AS1949490 (10 μM) impeded the transwell migration of MDA-MB-231 cell (*SI Appendix*, Fig. S5 *H* and *I*). Thus, the inhibition of the PI3K-SHIP2-SNX9 signaling axis suppresses the invasive cell migration.

Discussion

Phosphoinositide lipids are important signaling messengers to facilitate membrane compartmentalization and trigger a wide variety of cellular events. Here, we dissect the molecular pathway and examine the impact of $PI(3,4)P_2$ biogenesis on membrane trafficking, integrin receptor endocytosis, and invasive cell migration (Fig. 7). We find that $PI(3,4)P_2$, unlike other phosphoinositide lipids, is asymmetrically concentrated at the trailing edge of the invadopodium. The $PI(3,4)P_2$-rich compartment is actively reshaped and forms the invaginated membrane bud and tube in a SNX9- and microtubule-dependent manner, respectively. We further identify regulatory components of membrane tubulation, including AKTIP, Hook1, and microtubule retrograde motor dynein. Functionally, blocking the $PI(3,4)P_2$-mediated endocytosis pathway impedes integrin endocytosis, prevents the adhesion disassembly, and suppresses the invasive cell migration.

Using the approach of shRNA knockdown and rescue, we find that PIK3CA is critical to generate the intermediate product $PI(3,4,5)P_3$, which is then converted to $PI(3,4)P_2$ by the phosphoinositide 5-phosphatase SHIP2. The knockdown and chemical inhibition of PIK3CA result in the decrease of the $PI(3,4)P_2$ at the invadopodium but do not disrupt the invadopodium formation. Other isoforms of PI3K, such as PIK3CB, may compensate the essential function of PI3K when the expression of PIK3CA is suppressed. Likewise, the knockdown and chemical inhibition of SHIP2 results in the decrease of $PI(3,4)P_2$.

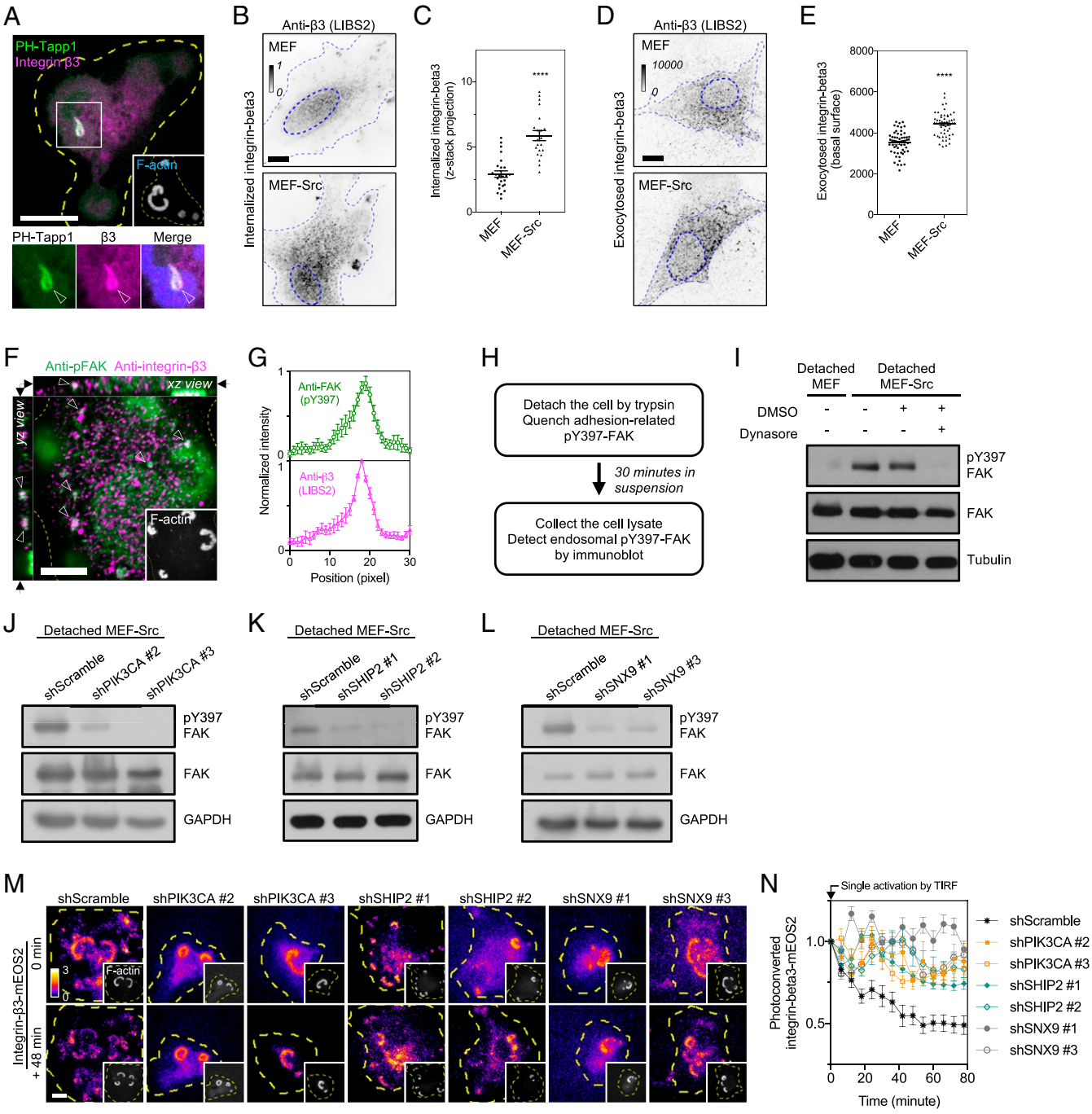

Fig. 5. PI(3,4)P_2-rich membrane invaginations promote the endocytosis of integrin-beta3 receptor. (*A*) Integrin-beta3-EBFP2 is enriched in the GFP-PH-Tapp1–positive membrane tube behind the invadopodium arc of MEF-Src (arrowheads). (*B*) More integrin-beta3 puncta, labeled by the conformation-specific LIBS2 antibody, are found in the cytoplasm of invadopodium-forming MEF-Src compared to that of wild-type MEF. Inverted images represent the projection of the confocal z-stack from 1 μm above the adhesion plane to the apex of the cell. (*C*) The ratio of internalized integrin-beta3 in wild-type MEF and MEF-Src. The statistical information is in *SI Appendix*, Table S1*G*. (*D*) MEF-Src exhibits a higher exocytosis level of integrin-beta3 than wild-type MEF. Inverted images represent the exocytosis level of integrin-beta3 using the antibody-based pulse–chase assay. (*E*) The intensity level of exocytosed integrin-beta3 in wild-type MEF and MEF-Src. The statistical information is in *SI Appendix*, Table S1*H*. (*F*) Puncta of anti-pY397-FAK and anti-integrin-beta3 colocalize in the cytoplasm of MEF-Src (arrowheads). The confocal image is shown at the z-position of the arrows indicated in xz and yz view. (*G*) The intensity profiles of anti-pY397-FAK and anti-integrin-beta3 (n = 11). (*H*) The schematic diagram of endosomal pY397-FAK detection. (*I*) The detection of endosomal pY397-FAK by the Western blot. Detached MEF-Src retains a higher level of endosomal pY397-FAK compared to detached wild-type MEF. The treatment with dynasore (20 μM) abolishes the endosomal pY397-FAK level in detached MEF-Src. (*J–L*) The knockdown of PIK3CA, SHIP2, and SNX9 suppress the level of endosomal pY397-FAK. (*M*) The turnover of TIRF-converted integrin-beta3-mEOS2 at the invadopodium. When PIK3CA, SHIP2, and SNX9 are knocked down, the photoconverted integrin-beta3-mEOS2 at the invadopodium is more stable than that in the scramble control. (*N*) The fold of change of photoconverted integrin-beta3-mEOS2 intensity at the invadopodium under the condition as indicated (n = 10 each). The invadopodium arc is labeled by F-actin marker LifeAct-miRFP703 (in *A* and *M*) or CF680R-phalloidin (in *F*). All experiments have been independently repeated three times. The graphs show mean ± SEM. Unpaired two-tailed Student's t test is applied for the statistical analysis. ****$P < 0.0001$ (Scale bars, 10 μm).

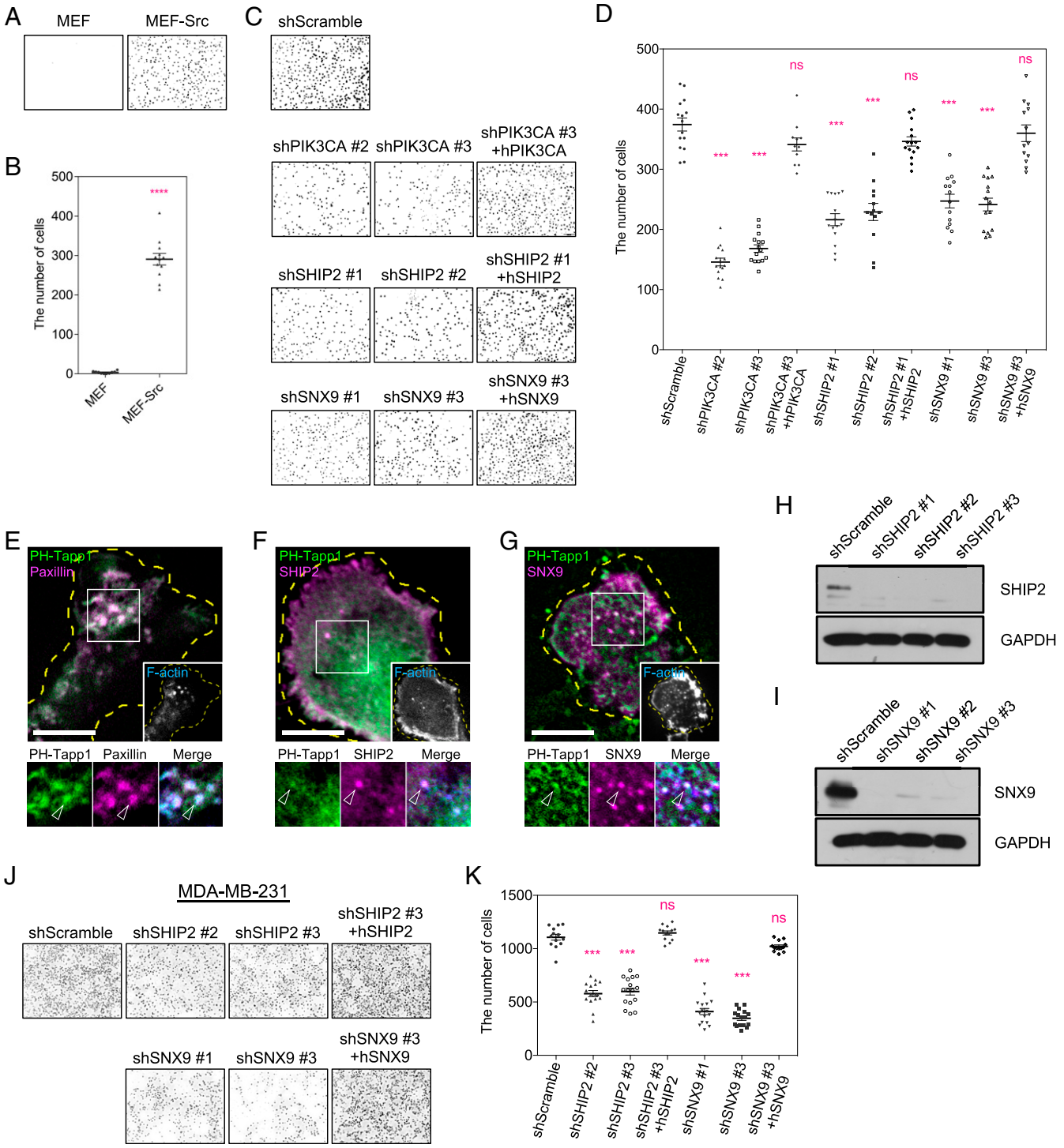

Fig. 6. Inhibitions of PI(3,4)P_2-mediated membrane invagination suppress the invasive migration of MEF-Src and MDA-MB231 cells. (*A*) Wild-type MEF and MEF-Src migrate through the Matrigel-coated transwell chamber. MEF-Src invades more than wild-type MEF. (*B*) The number of invaded wild-type MEF and MEF-Src. The statistical information is in *SI Appendix*, Table S1*I*. (*C*) The knockdown of PIK3CA, SHIP2, and SNX9 suppress the transwell invasion of MEF-Src compared to the scramble control. Reintroducing PIK3CA, SHIP2, and SNX9 restores the invasion of knockdown cells, respectively. (*D*) The number of invaded MEF-Src cells after knockdown and rescue as indicated. The statistical information is in *SI Appendix*, Table S1*J*. (*E*) GFP-PH-Tapp1 is enriched at the invadopodium of MDA-MB-231 cell (arrowheads). The invadopodium is identified by the F-actin core and the adhesion ring labeled by CF680R-phalloidin and RFP-paxillin, respectively. (*F* and *G*) mCherry-SHIP2 and mCherry-SNX9 colocalize with GFP-PH-Tapp1 at the invadopodium of MDA-MB-231 cells (arrowheads). (*H* and *I*) Western blot indicates the shRNA knockdown of SHIP2 and SNX9 in MDA-MB-231 cells. (*J*) The knockdown of SHIP2 and SNX9 suppress the transwell invasion of MDA-MB-231 cells. Reintroducing SHIP2 and SNX9 restores the invasion of knockdown cells. (*K*) The number of invaded MDA-MB-231 cells after knockdown and rescue as indicated. The statistical information is in *SI Appendix*, Table S1*K*. All experiments have been independently repeated three times. The graphs show mean ± SEM. Unpaired two-tailed Student's *t* test (in *B*) and one-way ANOVA with Dunnett's test (in *D* and *K*) are applied. Ns, $P > 0.1234$; ***$P < 0.0002$; ****$P < 0.0001$ (Scale bars, 10 μm).

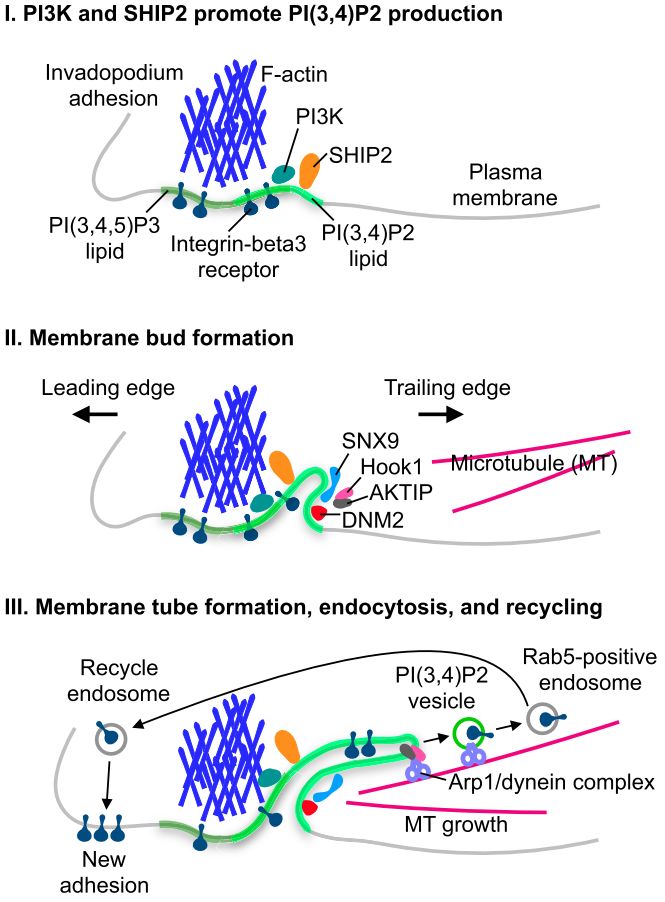

Fig. 7. $PI(3,4)P_2$ biogenesis at the invadopodium promotes integrin receptor endocytosis and cell migration. PI3K and SHIP2 regulate the production and the distribution of $PI(3,4)P_2$ at the trailing edge of invadopodium. The local enrichment of $PI(3,4)P_2$ recruits PX-BAR–domain protein SNX9 and DNM2. SNX9 contributes to the formation of the invaginated membrane bud that contains integrin-beta3 receptors. ATKIP and dynein activator Hook1 are located at the invaginated membrane bud and facilitate dynein-mediated membrane tube formation along the track of cortical microtubule. The emergence of membrane tubulation and internalization actively promote the endocytosis of integrin-beta3. Upraised endosomal recycling of integrin-beta3 further supports the new adhesion formation and enhances the invasive migration.

The distributions of SHIP2 and $PI(3,4)P_2$ are remarkably similar and are both enriched at the trailing edge of the invadopodium arc. Although other phosphoinositide 5-phosphatases, such as SYNJ2 and INPP5E, are found at the invadopodium, they can also dephosphorylate $PI(4,5)P_2$, which is the precursor of $PI(3,4,5)P_3$, and indirectly impede the production of $PI(3,4)P_2$ (15, 38, 39). Indeed, we find that the ectopic expression of SYNJ2 or INPP5E significantly suppresses the production of $PI(3,4)P_2$ at the invadopodium. While SHIP2 plays a critical role in the production and the asymmetrical enrichment of $PI(3,4)P_2$, other phosphoinositide 5-phosphatases may also contribute to the dephosphorylation of $PI(3,4,5)P_3$ at the invadopodium.

One unique event following the asymmetrical enrichment of $PI(3,4)P_2$ is the SNX9-dependent and clathrin-independent membrane invagination behind the invadopodium arc. SNX9 belongs to the family of PX-BAR–domain protein with a N-terminal SH3 domain and can promote DNM2-mediated membrane fission (40). We find that the knockdown of SNX9 inhibits the formation of membrane buds and suppresses the recruitment of DNM2 at the trailing edge of the invadopodium. The associations of SNX9 with $PI(3,4)P_2$, $PI(4,5)P_2$, and PI(3)P have been reported (41–43). Here, our data indicate that the recruitment of SNX9 is positively regulated by SHIP2-mediated $PI(3,4)P_2$ production and requires the PX-BAR domain. PI(3)P and $PI(4,5)P_2$ are not as concentrated as $PI(3,4)P_2$ at the invadopodium. Nevertheless, PI(3)P locally converted from $PI(3,4)P_2$ may also participate in the recruitment and activation of SNX9. Another $PI(3,4)P_2$ effector lamellipodin and N-BAR–domain protein endophilin have been reported to regulate clathrin-independent endocytosis of membrane receptors (44). However, we find that endophilin A1 is mainly located at the leading front, rather than the trailing edge of the invadopodium arc. Intriguingly, SNX9 and DNM2 remain at the membrane bud and the base of the membrane tube. The spatial confinement of SNX9 suggests the implication of nonlipid regulatory factors, such as membrane curvature modulation and protein scaffolding (45, 46).

We find that the formation of micrometer-long uncurving membrane tube is driven by microtubule and the retrograde motor dynein. As the tubulation events often repeatedly occur at the same location, factors that regulate microtubule dynamics, such as Kanks, liprins, and LL5β, may promote the targeting and stabilization of microtubules to the invadopodium (47). In addition, we find that protein complexes that associate with dynein, including AKTIP and Hook1 (30, 31), are dynamically enriched at the $PI(3,4)P_2$-rich membrane invagination. The elongation speed of the membrane tube can reach 160 nm/s. Previously, the mean speed of recombinant human dynein moving on surface-immobilized microtubules and microtubule sliding over surface-immobilized dynein are 159 ± 60 nm/s and 300 ± 110 nm/s, respectively (48, 49). In general, our observation agrees with the previous measurement. The enrichment of $PI(3,4)P_2$ is known to recruit Tks5 and to activate actin nucleation promoting factor cortactin (22). The slower elongation speed of the membrane tube in the live cell may result from the resistance from membrane tension and de novo F-actin assembly around the invaginated membrane tube that acts as stabilizing coatings and counterbalances the pulling force (50–53). While knockdown of AKTIP does not change the overall microtubule network (54) nor block the endocytosis of integrin receptors, AKTIP is needed for the recruitment of Hook1 to $PI(3,4)P_2$-rich membrane compartment. The absence of Hook1 may locally down-regulate dynein's motor activity and contribute to the accumulation of stationary $PI(3,4)P_2$-rich vesicles behind the invadopodium arc. Thus, microtubule/dynein-mediated membrane tubulation may accelerate the endocytosis process but does not play an essential role in $PI(3,4)P_2$-mediated endocytosis.

The elevated expression of SNX9 is often found in the metastatic mammary cancer (55). While the knockdown of SNX9 promotes the matrix degradation by suppressing the endocytosis of matrix metallopeptidase MT1-MMP, SNX9-depleted cells still exhibit the migration defect (56). Thus, apart from controlling the matrix degradation and MT1-MMP endocytosis, SNX9 must have other functional roles in regulating the cell motility. Indeed, SNX9 positively stimulates the angiogenesis by promoting the integrin trafficking in human umbilical vein endothelial cells (57). Here, we also find that the knockdown of SNX9 blocks integrin-beta3 endocytosis, suppresses the adhesion turnover, and impedes the invasion through a Matrigel-coated transwell chamber. Membrane receptors involved in the invadopodium, such as CD44, discoidin domain receptor, and other integrins, are likely to be regulated in the SNX9- and $PI(3,4)P_2$-dependent endocytosis pathway.

Invadopodia, like macrophage podosomes and focal adhesions, are integrin-mediated adhesions at the cell–matrix interface. The composition and the distribution of phosphoinositide lipids can play diverse roles in regulating the signaling event at the adhesion site. At the focal adhesion, the local production of $PI(4,5)P_2$ by PIPKI-γ90 facilitates the recruitment of talin and kindlin, which contribute to the integrin activation (58). Likewise, the biogenesis of $PI(3,4,5)P_3$ acts as the key factor to promote WASP

activation at the macrophage podosome (23). At the invadopodium, the enrichment of $PI(3,4)P_2$ and $PI(3,4,5)P_3$ is known to support F-actin stabilization by interacting with Tks5 and Myo1e, respectively (19, 22). Here, we report a functional role of $PI(3,4)P_2$ in promoting the SNX9 and microtubule-mediated membrane invagination and integrin trafficking. The turnover and recycling of integrin receptors are crucial for the cell migration. Factors that impede the $PI(3,4)P_2$ signaling and the membrane invagination may provide insights in inhibiting the cancer metastasis.

Materials and Methods

Cell Culture. RPTP$\alpha^{+/+}$ MEF cell line was a gift from Dr. Sap Jan, New York University School of Medicine. MDA-MB-231 cell line was obtained from the American Type Culture Collection. MEF, MEF-Src (MEF expressing the constitutively activated Src-Y530F mutant), and MDA-MB-231 cell lines were grown in Dulbecco's Modified Eagle Medium (DMEM) supplemented with 10% FBS (vol/vol), 100 unit/mL penicillin, and 100 μg/mL streptomycin (Thermo Fisher Scientific) in a 37 °C incubator with 5% CO_2. Unless otherwise stated, MEF-Src cells and the substrate coated with fibronectin (Thermo Fisher Scientific, 33016015) were used in the experiment.

Chemical Inhibitor. AS1949490 (3718) and dynasore (2897) were purchased from Tocris Bioscience. A66 (S2636), nocodazole (S2775), and wortmannin (S2758) were purchased from Selleckchem. The chemicals were dissolved in DMSO and were kept in the stock concentration 1,000 times higher than the working concentration. Before the application, the chemicals were then diluted to the working concentration with DMEM.

Antibodies. Primary antibodies included anti-pY416Src (CST 2101, 1:1,000 for Western blot [WB]), anti-Src (CST 2109, 1:1,000 for WB), anti-PIK3CA (Abcam ab40776; 1:100 for immunofluorescence [IF], 1:1,000 for WB), SHIP2 (Abcam ab70267; 1:100 for IF, 1:1,000 for WB), anti-AKTIP (Atlas Antibodies HPA046300; 1:1,000 for WB), anti-SNX9 (Atlas Antibodies HPA031410; 1:1,000 for WB), activated human integrin-β3 antibody (Millipore MABT27, LIBS2, epitope clone ab62; 1:50 for IF), anti-pFAK-Y397 (Thermo Fisher Scientific 44-624G; 1:100 for IF, 1:1,000 for WB), anti-FAK (Abcam ab40794; 1:1,000 for WB), anti-tubulin (CST 2146; 1:10000 for WB), and anti-GAPDH (Thermo Fisher Scientific AM4300; 1:10,000 for WB). Secondary antibodies included AF594-anti-mouse (Thermo Fisher Scientific A-21203; 1:1,000 for IF), AF594-anti-rabbit (Thermo Fisher Scientific A-21207; 1:1,000 for IF), AF488-anti-mouse (Thermo Fisher Scientific A-21202; 1:1,000 for IF) and AF488-anti-rabbit (Thermo Fisher Scientific A-21206; 1:1,000 for IF), anti-mouse horseradish peroxidase (HRP) (Santa Cruz sc-516102; 1:2,000 for WB), and anti-rabbit HRP (CST 7074; 1:2,000 for WB).

Fluorescence Microscopy. Fluorescent images were taken by an inverted spinning-disk confocal microscope or an inverted TIRF microscope. The spinning-disk confocal microscope (Nikon Eclipse Ti-E with Perkin-Elmer Ultraview VoX and Yokogawa CSU-X1) was controlled by Volocity software and was equipped with an electron-multiplying charge-coupled device (EMCCD) camera (Hamamatsu C9100-23B), a 100× oil immersion lens (numerical aperture [NA] = 1.45), acousto-optic tunable filter (AOTF)-controlled solid-state lasers (40 to 50 mW), and a piezo Z stage. The TIRF microscope (Zeiss Axio Observer Z1 with iLas2 TIRF module) was operated by MetaMorph software (Molecular Devices) and was equipped with an EMCCD camera (Photometrics Evolve 512), a 100× oil immersion lens (NA = 1.46), and AOTF-controlled solid-state lasers (50 to 100 mW). Emission filter settings were 445W60/615W70 (dual band-pass; EBFP and mCherry), 527W55 (EGFP), 485W60/705W90 (dual band-pass; cyan fluorescent protein and far-red probe). An environmental chamber (37 °C and 5% CO_2) was attached to the microscope for long-term time-lapse imaging. Phenol red-free DMEM with 100 unit/mL penicillin, 100 μg/mL streptomycin, and 20 mM Hepes was used as the imaging buffer for live-cell microscopy. Typically, the low laser power (less than 10%) and short exposure time (100 ms) were used to avoid nonspecific phototoxicity and pixel saturation. To avoid the overexpression artifact, cells with low expression level of fluorescent protein–tagged construct were examined. Raw images were acquired in the 16-bit format. Unless otherwise stated, each pixel approximately represented 132 nm under 100× oil immersion lens.

Lateral Distribution Analysis. The invadopodium arc was identified by the densely polymerized F-actin and imaged at the bottommost adhesion plane that was indicated by the plasma membrane marker CAAX. Unless otherwise stated, outside-in intensity line scans across the invadopodium were applied to measure the distribution of the protein of interest in ImageJ software. To compare the relative distribution among various lipid probes, acquired datasets were realigned so that the maximum fluorescence intensity in the F-actin channel was fixed at the position of the 101st pixel along the line scan. After normalization, the lateral distribution of the protein of interest relative to that of F-actin was then compared and plotted using GraphPad Prism software. In the quantification of membrane tube extension, the analysis of single representative cell was shown, and the dynamic changes of intensity profiles were consistent across multiple examples at similar temporal points.

Ratiometric Analysis of Enrichment Level. Cells with the prominent invadopodium arc were imaged with identical microscope configurations (laser output, exposure time, and camera electron-multiplying gain). To overcome the uneven membrane geometry, a z-stack of confocal images ranging from the bottommost adhesion plane to 3 μm above (200 nm per stack) were summed and formed a projected 32-bit image. The region of interest (ROI) of the invadopodium in the projected image was defined by the area with densely polymerized F-actin using ImageJ software. In the same cell, the ROI of noninvadopodium was defined by the following conditions: the region with the diffusive cytoplasmic pattern at the bottommost adhesion plane, with unnoticeable F-actin structures, and away from the cell nucleus. The intensity level at the invadopodium (I_{core}), cellular background ($I_{cytosol}$), and camera background ($I_{background}$) in the projected image were measured (Fig. 1*I*). The FOI of the protein of interest at the invadopodium was determined as "$(I_{core} - I_{cytosol})/(I_{cytosol} - I_{Background})$" and plotted using GraphPad Prism software. Pseudocolor ratiometric images were prepared with the same calculation above in ImageJ software, and the identical dynamic range was applied.

Quantification of Integrin-beta3 Endocytosis. The endocytosis of integrin-beta3 was detected by the conformation-specific antibody LIBS2 and was visualized by the confocal microscopy. A z-stack of confocal images ranging from 1 μm above the bottommost adhesion plane to the apex of the cell (200 nm per stack) were summed and formed a projected 32-bit image. The ROIs of the cytoplasm (excluding the nucleus) and a noncellular background in the projected image were assigned using ImageJ software. The mean intensity density within the ROIs of the cytoplasm ($I_{cytoplasm}$) and the noncellular background ($I_{background}$) in both the projected image and the image of the bottommost adhesion plane was also measured in ImageJ software. The ratio of internalized integrin-beta3 was defined as "$(I_{projected\ cytoplasm} - I_{projected\ background})/(I_{bottommost\ cytoplasm} - I_{bottommost\ background})$" and plotted using GraphPad Prism software.

Exocytosis Assay. MEF and MEF-Src cells were transfected with the human integrin-beta3 plasmid and plated on the fibronectin-coated glass. After 48 h, cells were cooled at 4 °C in serum-free DMEM containing 0.1% BSA and incubated with human integrin-beta3 antibody (LIBS2) for 1 h. The unbound antibody was washed away by serum-free DMEM at 4 °C. Cells were then maintained in the condition of serum-free DMEM containing 0.1% BSA for 2 h at 37 °C, in which the endocytosis of antibody-bound integrin-beta3 took place. Subsequently, the acid wash (0.5% glacial acetic acid and 0.5 M NaCl in pH = 3) was applied to remove the residual antibody left on the plasma membrane. The exocytosis was stimulated by replacing the culture medium with DMEM containing 10% FBS. After 5 min of serum stimulation, the cells were fixed, stained with secondary antibody and CF680R-phalloidinm, and then imaged by the confocal microscopy. Identical experiments without the initial incubation of LIBS2 were performed and acted as the control. The exocytosis level of integrin-beta3 receptor was determined by subtracting the intensity of the secondary antibody on the bottom layer of plasma membrane (summed between 0 and 400 nm, 200 nm per stack) of the control cells from that of the LIBS2-treated cells.

Photoconvertible Integrin-beta3-mEOS2 and Adhesion Turnover. A single photoactivation of 405 nm light by TIRF microscopy was applied to MEF-Src at the beginning in order to specifically convert the integrin-beta3-mEOS2 receptor at the cell–matrix interface. The MEF-Src cells with photoconverted integrin-beta3-mEOS2 (Set #1) were then imaged by the excitation of 561 nm laser and the emission filter of mCherry (615W70) every 3 min for 78 min (total 27 exposure counts). To measure the effect of photobeaching, another set of MEF-Src cells with the similar expression level of integrin-beta3-mEOS2 (Set #2) were also imaged 27 times with the same microscopy settings and a shorter time interval of 5 s. In both Set #1 and #2, the mean intensity of photoconverted integrin-beta3-mEOS2 within the ROI of the invadopodium (I_{core}) and the mean intensity of noncellular background

($I_{background}$) were quantified using Imaris software. The net intensity ($I_{core\text{-}BS}$) was defined by subtracting $I_{background}$ from I_{core}. In Set #2, the bleach correction function was generated by fitting the intensity changes of $I_{core\text{-}BS}^{Set\#2}$ with a two-phase decay model in GraphPad Prism software. In Set #1, the bleach-corrected intensity was then determined by the division of $I_{core\text{-}BS}^{Set\#1}$ by the bleach correction function and was plotted in GraphPad Prism software. Pseudocolor ratiometric images were prepared in ImageJ software using the same calculation above, and the identical dynamic range was applied.

Statistical Tests. All datasets contained at least three independent biological repeats. Statistical graphs with the mean and SEM were plotted using GraphPad Prism software. Statistical tests, including unpaired two-tailed Student's *t* test and one-way ANOVA with Dunnett's test, were performed using GraphPad Prism software. Detailed statistical information and *P* values can be found in *SI Appendix*, Table S1. Not significant (ns), $P > 0.1234$, $^{*}P < 0.0332$, $^{**}P < 0.0021$, $^{***}P < 0.0002$, and $^{****}P < 0.0001$.

Data Availability. All study data are included in the article and/or supporting information.

ACKNOWLEDGMENTS. This work was supported by Research Grant Council of Hong Kong, ECS 27110615 and GRF 17118620 (C.-h.Y.). We also thank Imaging & Flow Cytometry Core and Bioreagent Core in Centre for PanorOmic Sciences in Faculty of Medicine, University of Hong Kong.

1. Z. Sun, M. Costell, R. Fässler, Integrin activation by talin, kindlin and mechanical forces. *Nat. Cell Biol.* **21**, 25–31 (2019).
2. H. Wolfenson, B. Yang, M. P. Sheetz, Steps in mechanotransduction pathways that control cell morphology. *Annu. Rev. Physiol.* **81**, 585–605 (2019).
3. D. A. Murphy, S. A. Courtneidge, The 'ins' and 'outs' of podosomes and invadopodia: Characteristics, formation and function. *Nat. Rev. Mol. Cell Biol.* **12**, 413–426 (2011).
4. O. Destaing, M. R. Block, E. Planus, C. Albiges-Rizo, Invadosome regulation by adhesion signaling. *Curr. Opin. Cell Biol.* **23**, 597–606 (2011).
5. F. Cao, Y. Zhou, X. Liu, C. H. Yu, Podosome formation promotes plasma membrane invagination and integrin-β3 endocytosis on a viscous RGD-membrane. *Commun. Biol.* **3**, 117 (2020).
6. C. H. Yu, J. B. Law, M. Suryana, H. Y. Low, M. P. Sheetz, Early integrin binding to Arg-Gly-Asp peptide activates actin polymerization and contractile movement that stimulates outward translocation. *Proc. Natl. Acad. Sci. U.S.A.* **108**, 20585–20590 (2011).
7. B. P. Bouchet *et al*., Talin-KANK1 interaction controls the recruitment of cortical microtubule stabilizing complexes to focal adhesions. *eLife* **5**, e18124 (2016).
8. S. Seetharaman, S. Etienne-Manneville, Microtubules at focal adhesions–A double-edged sword. *J. Cell Sci.* **132**, jcs232843 (2019).
9. P. Moreno-Layseca, J. Icha, H. Hamidi, J. Ivaska, Integrin trafficking in cells and tissues. *Nat. Cell Biol.* **21**, 122–132 (2019).
10. N. R. Paul, G. Jacquemet, P. T. Caswell, Endocytic trafficking of integrins in cell migration. *Curr. Biol.* **25**, R1092–R1105 (2015).
11. T. Balla, Phosphoinositides: Tiny lipids with giant impact on cell regulation. *Physiol. Rev.* **93**, 1019–1137 (2013).
12. G. Di Paolo, P. De Camilli, Phosphoinositides in cell regulation and membrane dynamics. *Nature* **443**, 651–657 (2006).
13. S. Suetsugu, S. Kurisu, T. Takenawa, Dynamic shaping of cellular membranes by phospholipids and membrane-deforming proteins. *Physiol. Rev.* **94**, 1219–1248 (2014).
14. J. Saarikangas, H. Zhao, P. Lappalainen, Regulation of the actin cytoskeleton-plasma membrane interplay by phosphoinositides. *Physiol. Rev.* **90**, 259–289 (2010).
15. T. Sasaki *et al*., Mammalian phosphoinositide kinases and phosphatases. *Prog. Lipid Res.* **48**, 307–343 (2009).
16. P. T. Hawkins, L. R. Stephens, Emerging evidence of signalling roles for PI(3,4)P2 in Class I and II PI3K-regulated pathways. *Biochem. Soc. Trans.* **44**, 307–314 (2016).
17. M. J. Eramo, C. A. Mitchell, Regulation of PtdIns(3,4,5)P3/Akt signalling by inositol polyphosphate 5-phosphatases. *Biochem. Soc. Trans.* **44**, 240–252 (2016).
18. F. Gulluni, M. C. De Santis, J. P. Margaria, M. Martini, E. Hirsch, Class II PI3K functions in cell biology and disease. *Trends Cell Biol.* **29**, 339–359 (2019).
19. Y. Zhang *et al*., Tail domains of myosin-1e regulate phosphatidylinositol signaling and F-actin polymerization at the ventral layer of podosomes. *Mol. Biol. Cell* **30**, 622–635 (2019).
20. W. T. Chen, Proteolytic activity of specialized surface protrusions formed at rosette contact sites of transformed cells. *J. Exp. Zool.* **251**, 167–185 (1989).
21. G. R. Hammond, T. Balla, Polyphosphoinositide binding domains: Key to inositol lipid biology. *Biochim. Biophys. Acta* **1851**, 746–758 (2015).
22. T. Oikawa, T. Itoh, T. Takenawa, Sequential signals toward podosome formation in NIH-src cells. *J. Cell Biol.* **182**, 157–169 (2008).
23. Y. Zhou *et al*., Abl-mediated PI3K activation regulates macrophage podosome formation. *J. Cell Sci.* **133**, jcs234385 (2020).
24. B. D. Goulden *et al*., A high-avidity biosensor reveals plasma membrane PI(3,4)P_2 is predominantly a class I PI3K signaling product. *J. Cell Biol.* **218**, 1066–1079 (2019).
25. A. Suwa *et al*., Discovery and functional characterization of a novel small molecule inhibitor of the intracellular phosphatase, SHIP2. *Br. J. Pharmacol.* **158**, 879–887 (2009).
26. L. Chan Wah Hak *et al*., FBP17 and CIP4 recruit SHIP2 and lamellipodin to prime the plasma membrane for fast endophilin-mediated endocytosis. *Nat. Cell Biol.* **20**, 1023–1031 (2018).
27. G. F. W. Walpole, S. Grinstein, Endocytosis and the internalization of pathogenic organisms: Focus on phosphoinositides. *F1000 Res.* **9**, F1000 Faculty Rev-368 (2020).
28. S. Chowdhury, S. A. Ketcham, T. A. Schroer, G. C. Lander, Structural organization of the dynein-dynactin complex bound to microtubules. *Nat. Struct. Mol. Biol.* **22**, 345–347 (2015).
29. S. L. Reck-Peterson, W. B. Redwine, R. D. Vale, A. P. Carter, The cytoplasmic dynein transport machinery and its many cargoes. *Nat. Rev. Mol. Cell Biol.* **19**, 382–398 (2018).
30. I. Remy, S. W. Michnick, Regulation of apoptosis by the Ft1 protein, a new modulator of protein kinase B/Akt. *Mol. Cell. Biol.* **24**, 1493–1504 (2004).
31. L. Xu *et al*., An FTS/Hook/p107(FHIP) complex interacts with and promotes endosomal clustering by the homotypic vacuolar protein sorting complex. *Mol. Biol. Cell* **19**, 5059–5071 (2008).
32. H. Brzeska, J. Guag, K. Remmert, S. Chacko, E. D. Korn, An experimentally based computer search identifies unstructured membrane-binding sites in proteins: Application to class I myosins, PAKS, and CARMIL. *J. Biol. Chem.* **285**, 5738–5747 (2010).
33. N. Shin *et al*., SNX9 regulates tubular invagination of the plasma membrane through interaction with actin cytoskeleton and dynamin 2. *J. Cell Sci.* **121**, 1252–1263 (2008).
34. R. Lundmark, S. R. Carlsson, Regulated membrane recruitment of dynamin-2 mediated by sorting nexin 9. *J. Biol. Chem.* **279**, 42694–42702 (2004).
35. E. Macia *et al*., Dynasore, a cell-permeable inhibitor of dynamin. *Dev. Cell* **10**, 839–850 (2006).
36. B. D. Khalil *et al*., GPCR signaling mediates tumor metastasis via PI3Kβ. *Cancer Res.* **76**, 2944–2953 (2016).
37. R. J. Crowder *et al*., PIK3CA and PIK3CB inhibition produce synthetic lethality when combined with estrogen deprivation in estrogen receptor-positive breast cancer. *Cancer Res.* **69**, 3955–3962 (2009).
38. Y. Y. Chuang *et al*., Role of synaptojanin 2 in glioma cell migration and invasion. *Cancer Res.* **64**, 8271–8275 (2004).
39. H. Yamaguchi *et al*., Phosphatidylinositol 4,5-bisphosphate and PIP5-kinase Ialpha are required for invadopodia formation in human breast cancer cells. *Cancer Sci.* **101**, 1632–1638 (2010).
40. R. Lundmark, S. R. Carlsson, SNX9–A prelude to vesicle release. *J. Cell Sci.* **122**, 5–11 (2009).
41. Y. Posor *et al*., Spatiotemporal control of endocytosis by phosphatidylinositol-3,4-bisphosphate. *Nature* **499**, 233–237 (2013).
42. D. Yarar, M. C. Surka, M. C. Leonard, S. L. Schmid, SNX9 activities are regulated by multiple phosphoinositides through both PX and BAR domains. *Traffic* **9**, 133–146 (2008).
43. F. Daste *et al*., Control of actin polymerization via the coincidence of phosphoinositides and high membrane curvature. *J. Cell Biol.* **216**, 3745–3765 (2017).
44. E. Boucrot *et al*., Endophilin marks and controls a clathrin-independent endocytic pathway. *Nature* **517**, 460–465 (2015).
45. M. Simunovic *et al*., How curvature-generating proteins build scaffolds on membrane nanotubes. *Proc. Natl. Acad. Sci. U.S.A.* **113**, 11226–11231 (2016).
46. I. K. Jarsch, F. Daste, J. L. Gallop, Membrane curvature in cell biology: An integration of molecular mechanisms. *J. Cell Biol.* **214**, 375–387 (2016).
47. B. van der Vaart *et al*., CFEOM1-associated kinesin KIF21A is a cortical microtubule growth inhibitor. *Dev. Cell* **27**, 145–160 (2013).
48. M. A. Schlager, H. T. Hoang, L. Urnavicius, S. L. Bullock, A. P. Carter, In vitro reconstitution of a highly processive recombinant human dynein complex. *EMBO J.* **33**, 1855–1868 (2014).
49. R. J. McKenney, W. Huynh, M. E. Tanenbaum, G. Bhabha, R. D. Vale, Activation of cytoplasmic dynein motility by dynactin-cargo adapter complexes. *Science* **345**, 337–341 (2014).
50. E. Derivery *et al*., The Arp2/3 activator WASH controls the fission of endosomes through a large multiprotein complex. *Dev. Cell* **17**, 712–723 (2009).
51. Z. Shi, T. Baumgart, Membrane tension and peripheral protein density mediate membrane shape transitions. *Nat. Commun.* **6**, 5974 (2015).
52. P. Rangamani, K. K. Mandadap, G. Oster, Protein-induced membrane curvature alters local membrane tension. *Biophys. J.* **107**, 751–762 (2014).
53. C. Leduc, O. Campàs, J. F. Joanny, J. Prost, P. Bassereau, Mechanism of membrane nanotube formation by molecular motors. *Biochim. Biophys. Acta* **1798**, 1418–1426 (2010).
54. R. Burla *et al*., The telomeric protein AKTIP interacts with A- and B-type lamins and is involved in regulation of cellular senescence. *Open Biol.* **6**, 160103 (2016).
55. N. Bendris, S. L. Schmid, Endocytosis, metastasis and beyond: Multiple facets of SNX9. *Trends Cell Biol.* **27**, 189–200 (2017).
56. N. Bendris *et al*., Sorting nexin 9 negatively regulates invadopodia formation and function in cancer cells. *J. Cell Sci.* **129**, 2804–2816 (2016).
57. K. Tanigawa *et al*., SNX9 determines the surface levels of integrin β1 in vascular endothelial cells: Implication in poor prognosis of human colorectal cancers overexpressing SNX9. *J. Cell. Physiol.* **234**, 17280–17294 (2019).
58. G. Di Paolo *et al*., Recruitment and regulation of phosphatidylinositol phosphate kinase type 1 gamma by the FERM domain of talin. *Nature* **420**, 85–89 (2002).